

# Journal of Materials Chemistry A

Materials for energy and sustainability

Accepted Manuscript

This article can be cited before page numbers have been issued, to do this please use: S. Park and S. Y. Kim, *J. Mater. Chem. A*, 2026, DOI: 10.1039/D6TA01659F.



This is an Accepted Manuscript, which has been through the Royal Society of Chemistry peer review process and has been accepted for publication.

Accepted Manuscripts are published online shortly after acceptance, before technical editing, formatting and proof reading. Using this free service, authors can make their results available to the community, in citable form, before we publish the edited article. We will replace this Accepted Manuscript with the edited and formatted Advance Article as soon as it is available.

You can find more information about Accepted Manuscripts in the [Information for Authors](#).

Please note that technical editing may introduce minor changes to the text and/or graphics, which may alter content. The journal's standard [Terms & Conditions](#) and the [Ethical guidelines](#) still apply. In no event shall the Royal Society of Chemistry be held responsible for any errors or omissions in this Accepted Manuscript or any consequences arising from the use of any information it contains.

# Trade-off between O<sub>2</sub> activation and active-site regeneration on biaxially strained Co-doped MoS<sub>2</sub> monolayers: a density functional theory study

Soon-Dong Park<sup>a</sup> and Sung Youb Kim<sup>a,b\*</sup>

<sup>a</sup> Graduate School of Carbon Neutrality, Ulsan National Institute of Science and Technology,  
Ulsan 44919, Republic of Korea

<sup>b</sup> Graduate School of Semiconductor Materials and Devices Engineering, Ulsan National  
Institute of Science and Technology, Ulsan 44919, Republic of Korea

\* Corresponding author. E-mail: sykim@unist.ac.kr

## Abstract

Strain engineering can tune O<sub>2</sub> adsorption, activation, and dissociation on two-dimensional transition-metal dichalcogenide catalysts; however, its synergistic impact on O<sub>2</sub> activation/dissociation and active-site regeneration, both of which are required for sustained turnover, remains unclear. Herein, spin-polarized density functional theory is used to examine O<sub>2</sub> activation and regeneration at a substitutional Co site in monolayer MoS<sub>2</sub> (Co@V<sub>S</sub>). Phonon calculation results obtained for V<sub>S</sub> and Co@V<sub>S</sub> monolayers show the absence of imaginary modes at a 10% biaxial tensile strain (the highest strain examined), confirming dynamical stability at the upper bound of the studied strain window. With increasing strain, the O<sub>2</sub>-adsorbed Co@V<sub>S</sub> site undergoes a crossover between the S-preserved and S-reconstructed configurations near 4.5%, promoting the activation process. Consequently, O<sub>2</sub> dissociation preferentially follows a Mo-assisted pathway, yielding a deeply stabilized Co–O–Mo termination. The regeneration process assessed using an atomistic oxygen-migration proxy is



23 increasingly hindered by strain: between 4.5% and 5.0%, oxygen penetrates the lattice deeply  
24 and disrupts the site, whereas at a strain of 5.5%, oxygen removal is rate-limited by a large  
25 lateral diffusion barrier of 1.63 eV, consistent with the strengthened Co–O interactions. Overall,  
26 the applied strain facilitates O<sub>2</sub> dissociation, but it can also deepen oxide-like product wells and  
27 kinetically impede oxygen removal along the lattice-site hopping pathway. More broadly, the  
28 obtained results highlight an activation–regeneration trade-off that may be overlooked when  
29 strain engineering is primarily evaluated by activation descriptors, suggesting that optimal  
30 strain windows for strain-tuned single-atom catalysts should balance dissociation facilitation  
31 against the site recovery feasibility.

## 33 1. Introduction

34 Two-dimensional transition-metal dichalcogenides have emerged as versatile and tunable  
35 platforms for oxygen electrocatalysis.<sup>1–3</sup> They are widely used in air cathodes for alkaline Zn–  
36 air batteries,<sup>4,5</sup> oxygen reduction reaction (ORR) electrodes operating under both acidic and  
37 alkaline conditions,<sup>6–8</sup> and in the on-site synthesis of hydrogen peroxide via the two-electron  
38 ORR pathway ( $2e^-$ –ORR).<sup>9</sup> Recent advances have further demonstrated the potential of  
39 engineered two-dimensional catalysts for ORR through heterostructure design and defect  
40 engineering.<sup>10–12</sup> Among these materials, MoS<sub>2</sub> has been extensively studied, and ORR-related  
41 oxygen electrocatalytic activity was previously observed for MoSe<sub>2</sub>, WS<sub>2</sub>, and WSe<sub>2</sub>.<sup>4–9</sup>  
42 In MoS<sub>2</sub>, the electronically inert basal plane contrasts with chemically active point defects,  
43 where substitutional modifications can create metal–oxygen binding sites capable of activating



44 molecular oxygen ( $O_2$ ).<sup>13–15</sup> These  $O_2$ -active sites in  $MoS_2$  are generally categorized into edge  
45 sites and interior sulfur vacancies ( $V_S$ ). In large-area films, sulfur vacancies are formed during  
46 chemical vapor deposition or liquid-phase exfoliation with areal densities ranging from  $10^{10}$  to  
47  $10^{13} \text{ cm}^{-2}$ , as confirmed by aberration-corrected scanning transmission electron microscopy  
48 combined with electron energy loss spectroscopy.<sup>16,17</sup> In small-area single crystals, edge sites  
49 typically predominate, whereas in wafer-scale films,  $V_S$  often serve as the primary active  
50 sites.<sup>16,17</sup> Theoretically,  $O_2$  dissociation on the pristine  $MoS_2$  basal plane requires a high energy  
51 barrier ( $\sim 1.6 \text{ eV}$ ); however, the presence of a  $V_S$  reduces this barrier by half to approximately  
52  $0.8 \text{ eV}$ , making the dissociation process more feasible.<sup>18</sup> Meanwhile, sustained  $O_2$  turnover  
53 necessitates the continuous regeneration of clean vacancies, because a vacancy that has reacted  
54 with oxygen becomes difficult to reactivate. Density functional theory (DFT) and spectroscopic  
55 studies have demonstrated that an oxygen atom occupying a sulfur vacancy in monolayer  $MoS_2$   
56 is strongly stabilized, with adsorption energies around  $-4 \text{ eV}$  and repair energies of  
57 approximately  $2\text{--}4 \text{ eV}$  relative to those of bare  $V_S$ . The resulting oxygen-filled defects  
58 eliminate vacancy-derived mid-gap states, restore a nearly pristine band structure, and yield  
59 long-lived photoluminescence recovery, all of which are consistent with a thermodynamically  
60 deep, electronically passivated state that is unlikely to participate in further  $O_2$  activation  
61 cycles.<sup>19–21</sup>

62 Transition-metal substitution—particularly Co substitution at a sulfur vacancy ( $Co@V_S$ )—has  
63 been proposed as an effective strategy for overcoming this limitation.<sup>14,15,22–24</sup> In these Co-  
64 decorated vacancies, the Co atom forms a strongly bound single-atom site and activates the  
65 adsorbed  $O_2$  species through the metal–oxygen hybridization and partially occupied Co  $d$  states  
66 near the Fermi level. This interaction promotes  $\pi^*$  back-donation and weakens the O–O



67 bond.<sup>14,15,22,23</sup> Among the  $3d$  dopants, Co is especially attractive owing to its favorable ionic  
68 radius and electronic configuration, which ensure structural stability within the  $\text{MoS}_2$  lattice.  
69 Additionally, its partially filled  $d$  orbitals provide a balanced oxygen-binding strength and  
70 experimentally verified catalytic activity in oxygen-involving reactions.<sup>25,26</sup> Besides  
71 substitutional doping, the further tuning of the local electronic environment near  $V_S$  offers a  
72 promising approach to controlling the  $\text{O}_2$  reactivity. Previous studies on Co, Ni, Fe, and Cu  
73 dopants have demonstrated strong anchoring of transition metal atoms at  $V_S$  and significant  
74 reorganization of the local electronic structure.<sup>13–15,22,23</sup> Notably,  $\text{Co}@V_S$  stands out because it  
75 (i) forms a thermodynamically stable single-atom site at the vacancy, (ii) hosts  $d$  states near the  
76 Fermi level that efficiently couple to the  $\text{O}_2 \pi^*$  manifold, and (iii) weakens the O–O bond  
77 without causing excessive oxygen over-binding,<sup>13–15,22,23</sup> making it an ideal platform for strain-  
78 tunable oxygen activation.

79 Biaxial tensile strain, which can reach approximately 5–6% in suspended monolayer  $\text{MoS}_2$   
80 membranes and 1% in polymer-supported devices, further modulates band edges and orbital  
81 hybridization.<sup>27–30</sup> Strain engineering can induce direct-to-indirect bandgap transitions and  
82 alter the  $\text{Mo}-d / \text{S}-p$  hybridization patterns near both the valence band maximum and  
83 conduction band minimum.<sup>31,32</sup> This pronounced strain sensitivity of the  $\text{MoS}_2$  lattice suggests  
84 that in our  $\text{Co}@V_S-\text{O}_2$  system, biaxial strain can modulate the three-way orbital coupling  
85 among the  $\text{MoS}_2$  lattice, Co dopant, and  $\text{O}_2 \pi^*$  manifold. However, the synergistic effect of the  
86 transition metal substitution ( $\text{Co}@V_S$ ) and biaxial strain on  $\text{O}_2$  activation and dissociation in  
87  $\text{MoS}_2$  has not been systematically explored yet. Most previous strain engineering studies focus  
88 on the activation-related descriptors, whereas the kinetic feasibility of active-site regeneration  
89 following  $\text{O}_2$  dissociation has received significantly less attention from researchers. Therefore,



90 in this work, we investigated how biaxial tensile strain influenced the electronic structure of  
91 Co@V<sub>S</sub> and its interaction with adsorbed O<sub>2</sub> species. By analyzing structural, vibrational, and  
92 electronic responses under strain, we clarified how lattice deformation affected the O–O  
93 activation process and associated dissociation pathway and further examined the energetics of  
94 active-site regeneration to provide a comprehensive view of the full catalytic cycle. The present  
95 analysis focuses on the intrinsic, potential-independent structural energetics of the activation–  
96 regeneration balance; the effects of electrode potential, solvation, and proton–electron transfer,  
97 which are important under realistic electrochemical conditions, are beyond the scope of this  
98 work.

## 100 2. Computational method

101 We performed spin-polarized DFT calculations to evaluate the structural stability of Co-doped  
102 MoS<sub>2</sub> monolayers (1H phase) under tensile strain and explore the bonding characteristics of  
103 adsorbed O<sub>2</sub> species, including the energetics of the O–O bond dissociation. All calculations  
104 utilized the plane-wave projector augmented-wave (PAW) method<sup>33,34</sup> implemented in the  
105 Vienna Ab initio Simulation Package (VASP)<sup>35,36</sup> with exchange–correlation effects described  
106 by the GGA–PBE functional.<sup>37</sup> A plane-wave kinetic energy cutoff of 500 eV was applied.  
107 Geometry optimizations proceeded until residual atomic forces were below 0.01 eV Å<sup>-1</sup>, and  
108 the electronic energy convergence was set to 10<sup>-6</sup> eV. Stress–strain calculations for the pristine  
109 MoS<sub>2</sub> unit cell were performed using an 8 × 6 × 1 Monkhorst–Pack<sup>38</sup> k-point mesh. In contrast,  
110 adsorption and nudged elastic band (NEB) calculations for the 5 × 3 supercell employed a 2 ×  
111 2 × 1 mesh. For partial density of states (PDOS) calculations, a denser 6 × 6 × 1 mesh was



112 utilized, while a  $3 \times 3 \times 1$  mesh was applied for Bader charge and crystal orbital Hamilton  
113 population (COHP)<sup>39</sup> analyses. Geometry optimizations and NEB barrier calculations were  
114 performed within an orthorhombic supercell under equal biaxial in-plane strain. The  
115 orthorhombic  $5 \times 3$  cell is a standard rectangular representation of the hexagonal MoS<sub>2</sub> lattice  
116 ( $a_{\text{orth}} = a_{\text{hex}}$ ,  $b_{\text{orth}} = \sqrt{3} \times a_{\text{hex}}$ ). Because the two lattice vectors are related by a fixed geometric  
117 factor, uniform scaling by  $(1 + \epsilon)$  preserves the hexagonal symmetry of the underlying lattice;  
118 thus, the strain condition  $\epsilon_x = \epsilon_y$  in the orthorhombic frame is equivalent to isotropic biaxial  
119 strain in the hexagonal frame. To facilitate a comparison with previous studies and avoid  
120 artifacts from Brillouin zone folding, phonon dispersions were computed for the hexagonal  
121 primitive cell under the same biaxial strain and plotted along the  $\Gamma$ –M–K– $\Gamma$  path. As shown in  
122 Figure 1(a), a rectangular unit cell of the MoS<sub>2</sub> monolayer was adopted and expanded into a  $5$   
123  $\times 3 \times 1$  supercell containing 90 framework atoms. Co doping was performed by substituting a  
124 Co atom at a sulfur vacancy site (Co@V<sub>S</sub>), corresponding to approximately 1.7% doping on  
125 the chalcogen sublattice. Subsequently, an O<sub>2</sub> molecule was adsorbed at this Co site, resulting  
126 in a 92-atom Co@V<sub>S</sub>–O<sub>2</sub> system (containing 30 Mo, 59 S, 1 Co, and 2 O atoms; see Figure  
127 1(a)). Periodic boundary conditions were applied, and a vacuum spacing of approximately 15  
128 Å was introduced along the surface normal (z direction) to prevent spurious interactions  
129 between periodically repeated slabs. The in-plane stress of the MoS<sub>2</sub> monolayer was derived  
130 from the cell-averaged three-dimensional (3D) virial stress and reported as a 3D in-plane stress,  
131 using a fixed effective thickness  $d = 0.615$  nm (half the interlayer spacing of bulk MoS<sub>2</sub>) for  
132 consistency with a prior work.<sup>27</sup> Note that the stress values expressed in GPa are conventional  
133 3D-equivalent quantities that depend on the assumed effective thickness and therefore do not  
134 represent an intrinsic 2D mechanical property. All physically meaningful analyses in this work,  
135 including the S-preserved (SP)–S-reconstructed (SR) transition (hereafter referred to as SP–SR



136 transition), dissociation barriers, and regeneration energetics, are parameterized by strain (a  
137 dimensionless, thickness-independent quantity) rather than by stress. For reference, 2D stress  
138 can be obtained as  $\sigma_{2D}$  (N/m) =  $\sigma_{3D}$  (GPa)  $\times$   $d$ , where  $d = 0.615$  nm is the effective thickness  
139 adopted herein. Isotropic biaxial tensile strain ( $\epsilon_x = \epsilon_y$ ) was imposed by uniformly scaling the  
140 in-plane lattice parameters by  $(1 + \epsilon)$ , followed by the full relaxation of all internal atomic  
141 coordinates at each strain.

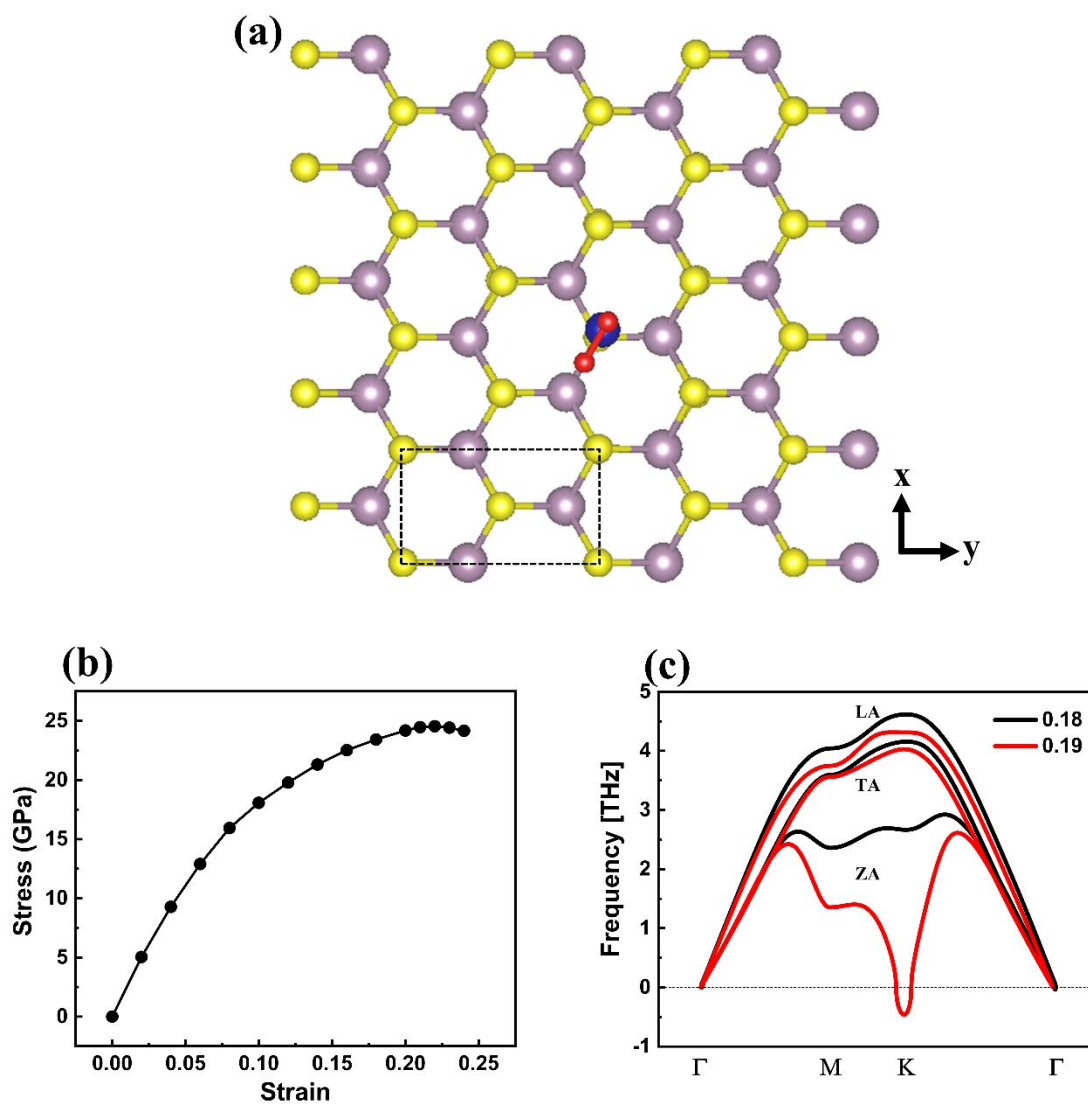
142 Vibrational properties were calculated using a finite displacement method and subsequently  
143 processed with Phonopy software<sup>40,41</sup> to obtain phonon dispersion curves. Bader charge  
144 analysis was conducted according to the standard partitioning scheme.<sup>42–44</sup> COHP curves were  
145 generated with LOBSTER software<sup>45</sup> utilizing appropriate PAW-based projection sets, and the  
146 projected COHP (pCOHP) was analyzed. Following the standard convention, the negative  
147 values  $-pCOHP$  were plotted so that the positive and negative peaks corresponded to the  
148 bonding and antibonding contributions, respectively. Minimum-energy reaction pathways,  
149 including the O–O dissociation barrier, were determined using the NEB method with the  
150 climbing-image variant (CI-NEB).<sup>46–48</sup> For each elementary step, five intermediate images  
151 were inserted between the optimized initial and final states. The images along the reaction path  
152 were optimized until the maximum force became less than or equal to  $0.02$  eV  $\text{\AA}^{-1}$ . To assess  
153 the sensitivity of the main conclusions to the choice of exchange-correlation functional,  
154 PBE+U calculations were performed for the  $\text{Co}@V_S\text{-O}_2$  system using an effective Hubbard  
155 parameter  $U_{\text{eff}} = 3.3$  eV for the Co  $d$  electrons, consistent with the value employed by Oh et  
156 al.<sup>49</sup> for Co  $3d$  electrons in TMD-based heterostructures, originally adopted from Grimaud et  
157 al.<sup>50</sup>; the Hubbard correction was applied solely to the Co dopant, as the localized  $d$  states at  
158 the substitutional site are the primary concern for self-interaction errors (Table S3 in the ESI).



159

160

## 3. Results and discussion



161

162 **Figure 1.** (a)  $(5 \times 3)$  supercell structure of Co-doped monolayer MoS<sub>2</sub> with an O<sub>2</sub> molecule  
 163 adsorbed at the substitutional Co site; the dotted box indicates the pristine unit cell. (b) In-plane  
 164 stress–strain curve of the pristine unit cell recorded under incremental biaxial tensile loading.  
 165 The stress values are conventional 3D-equivalent quantities obtained using an effective  
 166 thickness of 0.615 nm; see the Computational Method section for details. (c) Phonon  
 167 dispersions obtained at strains  $\varepsilon = 0.18$  and 0.19. In (a), the purple, yellow, blue, and red spheres  
 168 represent Mo, S, Co, and O atoms, respectively.

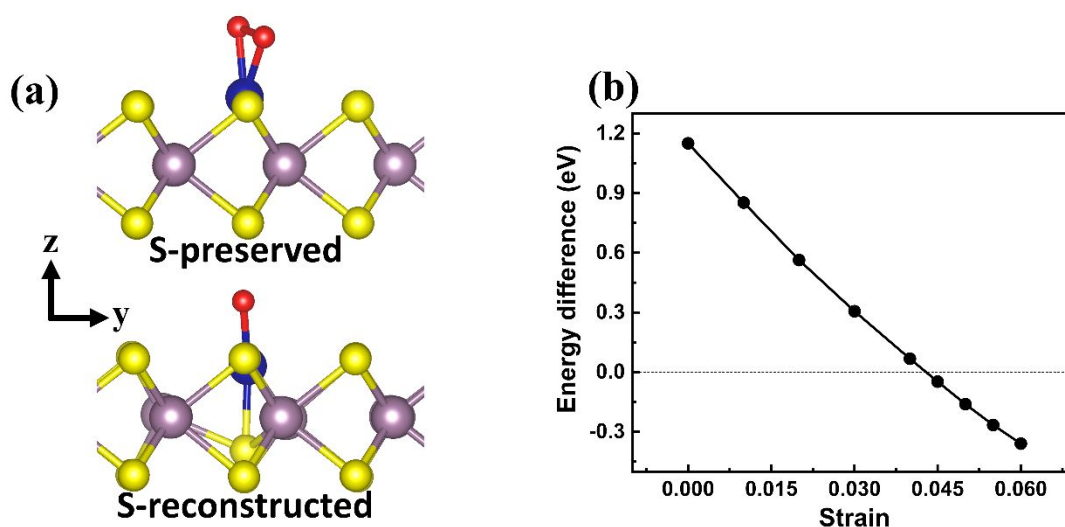


169

170 Figure 1(a) shows the  $5 \times 3$  supercell of Co-doped monolayer  $\text{MoS}_2$  with an  $\text{O}_2$  molecule  
171 adsorbed at the substitutional Co site; the dotted box highlights the pristine  $\text{MoS}_2$  unit cell. To  
172 examine the effect of strain on  $\text{O}_2$  dissociation at this Co-doped site, we first applied  
173 incremental biaxial tensile strain to the pristine  $\text{MoS}_2$  unit cell which has the in-plane lattice  
174 parameters  $a = 3.183 \text{ \AA}$  and  $b = 5.514 \text{ \AA}$ , and calculated the corresponding in-plane stress. The  
175 resulting biaxial stress–strain relationship is summarized in Figure 1(b): as the tensile strain  $\epsilon$   
176 increases, the in-plane stress  $\sigma$  initially rises nonlinearly, reaches a peak, and then decreases.  
177 At  $\epsilon = 0.22$ , the stress attains the maximum value  $\sigma_{\text{max}} = 24.54 \text{ GPa}$ , representing the theoretical  
178 biaxial stress derived from the homogeneous  $\sigma$ – $\epsilon$  curve without considering lattice instabilities.  
179 However, a detailed evaluation of dynamical stability based on the phonon dispersions  
180 presented in Figure 1(c) reveals that the pristine  $\text{MoS}_2$  monolayer becomes unstable at a lower  
181 strain. No imaginary phonon frequencies are observed at  $\epsilon = 0.18$ ; however, at  $\epsilon = 0.19$ , the  
182 out-of-plane acoustic (ZA) branch exhibits imaginary frequencies at the K point, indicating the  
183 onset of phonon instability. These results suggest that the critical strain for the onset of  
184 dynamical instability lies between  $\epsilon = 0.18$  and  $0.19$ , corresponding to a stress of approximately  
185  $23.42 \text{ GPa}$ . Therefore, we adopted this value as the ideal biaxial strength of the pristine  $\text{MoS}_2$   
186 monolayer limited by the onset of phonon instability, corresponding to a 2D stress of  
187 approximately  $14.4 \text{ N/m}$ . This estimate is in good agreement with the results of previous studies.  
188 Li et al.<sup>27</sup> reported an ideal biaxial strength of  $23.8 \text{ GPa}$  at  $\epsilon \approx 0.20$  and identified the onset of  
189 phonon instability at the K point, while Cooper et al.<sup>51</sup> constructed a biaxial stress–strain curve  
190 in quantitative agreement with the results reported by Li et al. The overall shape of the stress–  
191 strain curve obtained here, an initial nonlinear rise followed by a peak and subsequent softening,



192 is consistent with both of these prior reports, and the phonon-instability threshold identified at  
193 the K point likewise agrees with the instability mode reported by Li et al., confirming the  
194 reliability of the present computational setup for describing the mechanical response of  
195 monolayer MoS<sub>2</sub> under biaxial tension. Furthermore, experimental studies have demonstrated  
196 that suspended monolayer MoS<sub>2</sub> membranes can sustain biaxial tensile strains of over 5%  
197 before rupture and exhibit breaking strains of 6–11% during nanoindentation.<sup>29,52</sup> These  
198 experimental findings motivated us to explore strains up to 10%, and our phonon-stability  
199 analysis confirmed that the biaxial strain window of 4.5–10% examined in the present work  
200 remained dynamically stable, providing a substantial safety margin relative to the ideal phonon-  
201 instability threshold. Additionally, phonon dispersion calculations conducted for monolayer  
202 MoS<sub>2</sub> containing a single sulfur vacancy and the corresponding Co-substituted structure at a  
203 10% biaxial tensile strain revealed the absence of imaginary modes along the  $\Gamma$ -M-K- $\Gamma$  path  
204 (Figure S1). These results confirmed that the defected and Co-doped monolayers remained  
205 dynamically stable even at the highest strain applied in this work.



207



208 **Figure 2.** (a) Side views of the SP and SR configurations of the O<sub>2</sub> molecule adsorbed at the  
 209 Co substitutional site (Co@V<sub>S</sub>) in monolayer MoS<sub>2</sub>. (b) Relative energy difference between  
 210 the SR and SP configurations ( $E_{SR} - E_{SP}$ ), calculated per 5×3 supercell, as a function of biaxial  
 211 strain. The energy crossover at  $\epsilon = 4.5\%$  indicates the strain at which the SR structure becomes  
 212 thermodynamically favored. In (a), the purple, yellow, blue, and red spheres represent Mo, S,  
 213 Co, and O atoms, respectively.

214

215 **Table 1.** Structural distances (in Å) for O<sub>2</sub> adsorbed at a substitutional Co site in monolayer  
 216 MoS<sub>2</sub> under the biaxial tensile strain. The Co–O bond lengths, O–O separation, and Co–S  
 217 distance between the Co atom and S atom located directly beneath it in the lower S sublayer  
 218 are provided for each strain. Up to a 4% strain, the data correspond to the SP configuration,  
 219 while at a 4.5% strain and above, they represent the SR configuration, which becomes  
 220 energetically favorable at a higher strain. Additionally, the metastable SP structure at a 4.5%  
 221 strain is included to illustrate the structural changes occurring during the SP–SR transition.

Configuration	Strain	Co–O1	Co–O2	O1–O2	Co–S
SP	0.000	1.895	1.893	1.357	3.469
	0.020	1.878	1.883	1.360	3.367
	0.040	1.862	1.878	1.364	3.258
	0.045	1.857	1.877	1.364	3.230
SR	0.045	1.828	1.828	1.380	2.194
	0.075	1.826	1.826	1.374	2.148
	0.100	1.825	1.825	1.373	2.117

222

223 Using the strained pristine lattices obtained earlier as the starting points, Co-doped MoS<sub>2</sub>  
 224 supercells were constructed next. For each strain, the relaxed primitive cell was expanded into  
 225 a 5×3 supercell, where a single S atom was replaced with a Co atom to create a substitutional

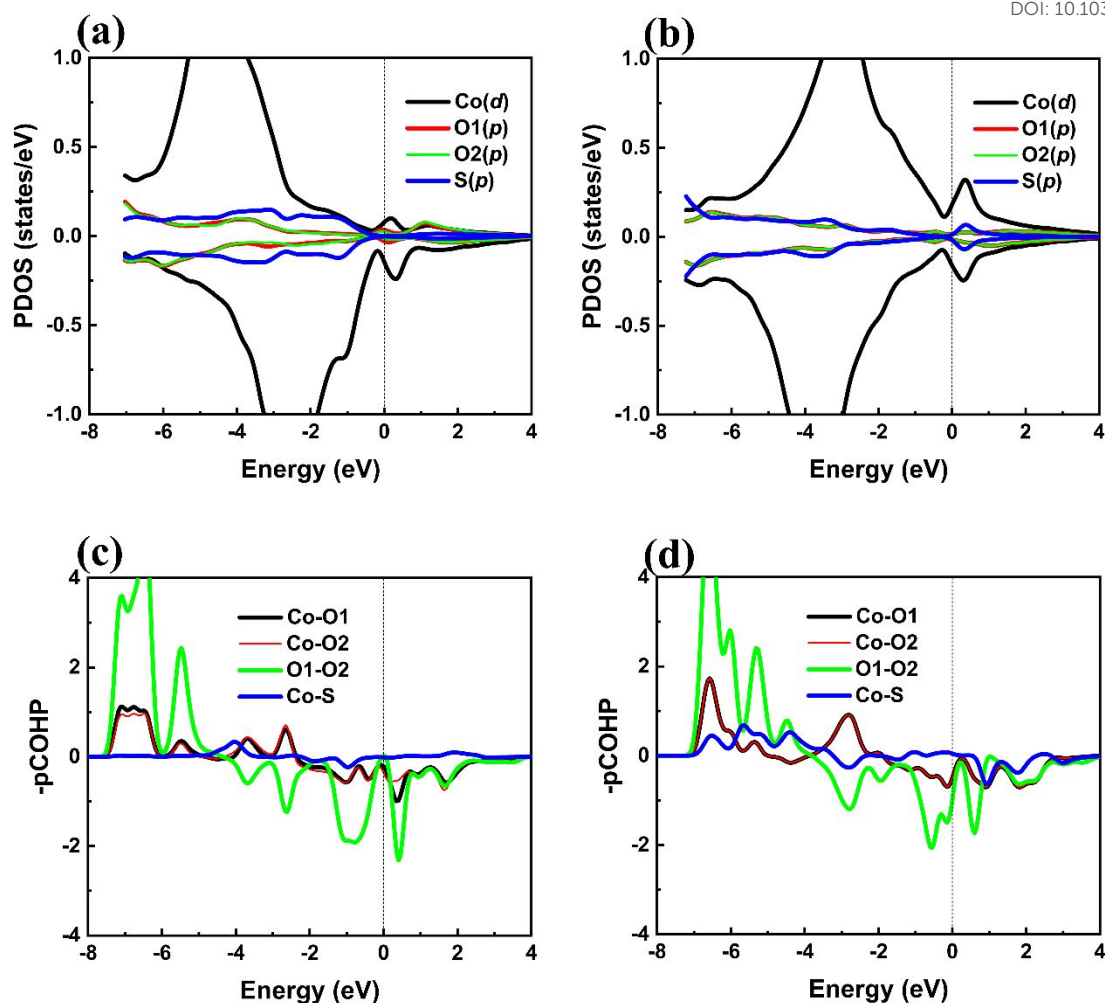


226 Co atom at a sulfur site (Co@V<sub>S</sub>). The resulting Co-doped structure with an O<sub>2</sub> molecule  
227 adsorbed at the Co@V<sub>S</sub> site is shown in Figure 1(a); at each strain, all internal atomic  
228 coordinates were fully relaxed. The adsorption of O<sub>2</sub> at this Co site in 1H-MoS<sub>2</sub> resulted in  
229 two distinct local minima, which corresponded to the SP and SR configurations (Figure 2(a)).  
230 At biaxial tensile strains up to approximately 6%, structural relaxations can converge to either  
231 the SP or SR local minimum. However, beyond a strain of approximately 6%, the system  
232 consistently converges to the SR configuration, and the SP structure can no longer be  
233 maintained. The most notable difference between these two configurations lies in the Co-S  
234 bond length. To compare them more directly, we focus on the 4.5% strain case in Table 1: the  
235 SP configuration retains a largely intact lower S sublayer and exhibits a relatively long Co-S  
236 separation of approximately 3.23 Å. In this state, the Co atom is not deeply embedded into the  
237 MoS<sub>2</sub> lattice but instead protrudes above the surface in an adatom-like geometry. In contrast,  
238 the SR configuration at the same strain demonstrates an upward displacement of the nearest-  
239 neighbor S atom and corresponding sinking of the Co atom into the MoS<sub>2</sub> monolayer. This  
240 results in a shortened Co-S bond length of approximately 2.19 Å with the Co atom more deeply  
241 embedded into the lattice. This substrate-mediated reconstruction significantly alters the ligand  
242 field and local electronic environment around the Co center, as further supported by the results  
243 of PDOS and COHP analyses discussed in the next paragraph. At biaxial tensile strains up to  
244 4%, the SP structure is consistently more stable than the SR structure; however, the energy  
245 difference between them gradually decreases and reverses at a 4.5% strain, when the SR  
246 configuration becomes energetically favored (Figure 2(b)). To illustrate this trend and the  
247 related transition point, Table 1 summarizes the geometric parameters of the lowest-energy  
248 configurations computed at all strains. At a 4.5% strain, the metastable SP configuration is also  
249 listed to highlight structural changes across the SP-SR transition. The O-O bond lengths



250 reported in Table 1 already exceed 1.30 Å at both reference strains — 0% (SP) and 4.5% (SR)  
251 — and the corresponding O–O stretching frequencies in Table S1 are strongly red-shifted from  
252 the experimental gas-phase value (1.207 Å and 1556 cm<sup>-1</sup><sup>53</sup>) to approximately 1050 cm<sup>-1</sup> for  
253 the SP configuration and 980–990 cm<sup>-1</sup> for the SR configuration. This indicates that in both  
254 cases, the adsorbed O<sub>2</sub> molecules exhibit the characteristics of superoxo-like O<sub>2</sub> species. In  
255 transition-metal–dioxygen complexes, the simultaneous elongation of the O–O bond and  
256 reduction of the stretching frequency are characteristic signatures of superoxo-like O<sub>2</sub> species,  
257 which are commonly associated with the partial filling of the O–O π\* antibonding orbitals—  
258 that is, a partially activated O<sub>2</sub> species.<sup>54</sup> According to Table 1, the O–O bond length within  
259 the SP branch (0–4% strain) increases gradually with biaxial tension and becomes further  
260 elongated in the SR configuration at a 4.5% strain, reflecting a systematic enhancement in the  
261 activation of the adsorbed O<sub>2</sub> species. When the strain increases from 4.0% to 4.5%, the  
262 additional elongation and activation of the O–O bond originate not only from the increased  
263 strain itself but, more importantly, from the accompanying transition from the SP to SR  
264 configuration. Thus, ε ≈ 4.5% marks a qualitative transition from a gently strain-activated SP  
265 branch to a reconstructed SR branch with distinctly stronger O<sub>2</sub> activation, providing a natural  
266 dividing line for the subsequent electronic structure and reaction-pathway analyses.





267

268 **Figure 3.** Spin-resolved PDOS and  $-p\text{COHP}$  analyses of the  $\text{O}_2$  molecule adsorbed on  $\text{Co@V}_5$   
 269 under a biaxial tensile strain of  $\varepsilon = 4.5\%$ . The spin-resolved PDOS calculated for the (a) SP  
 270 and (b) SR configurations, with the positive and negative values indicating the spin-up and  
 271 spin-down components, respectively. The Fermi level is set at zero energy. The  $-p\text{COHP}$   
 272 curves obtained for selected Co–O, O–O, and Co–S bonds in the (c) SP and (d) SR  
 273 configurations; here, the positive and negative values correspond to the bonding and  
 274 antibonding contributions, respectively.

275

276 **Table 2.** Integrated  $-\text{ICOHP}$  (eV per bond) values for selected bonds surrounding adsorbed  $\text{O}_2$   
 277 in the SP and SR configurations at  $\varepsilon = 4.5\%$ . The higher  $-\text{ICOHP}$  values correspond to the  
 278 stronger covalent interactions.



Configuration	Co–O1	Co–O2	O1–O2	Co–S
SP	2.145	1.889	11.354	0.097
SR	2.368	2.373	10.776	2.038

279

280 To further clarify these strain-induced structural changes, we compared the spin-resolved  
 281 PDOS of the substitutional Co center, adsorbed O<sub>2</sub> molecule, and S atom located directly  
 282 beneath the Co site, along with the corresponding –pCOHP spectra for the two local minima  
 283 coexisting at the SP–SR crossover strain  $\epsilon = 4.5\%$  (Figure 3). In the SP configuration at  $\epsilon = 4.5\%$   
 284 (Figures 3(a) and 3(c)), the Co *d* manifold remains strongly spin-polarized, exhibiting large  
 285 majority-spin peaks with energies several eV below the Fermi level and comparatively weak  
 286 minority-spin intensity near the Fermi level. The *p* states of O1 and O2 exhibit only modest  
 287 weights around the Fermi level, while the S *p* contribution is negligible, which is consistent  
 288 with a superoxo-like O<sub>2</sub> species coupled to a high-spin Co center with a total magnetic moment  
 289 of approximately 3  $\mu_B$ . From a ligand-field perspective, this SP configuration corresponds to a  
 290 relatively weak ligand field around the Co center that stabilizes the high-spin state. The  
 291 –pCOHP curves depicted in Figure 3(c) support this interpretation: the O1–O2 bond shows  
 292 relatively large positive (bonding) contributions that are well below the Fermi level along with  
 293 the pronounced antibonding features near the Fermi level. Meanwhile, the Co–O1 and Co–O2  
 294 bonds are moderately bonding, and the Co–S interaction is nearly negligible in a good  
 295 agreement with the large –ICOHP value obtained for O–O and much smaller values determined  
 296 for Co–O and Co–S (Table 2). In the SR configuration at the same strain (Figures 3(b) and (d)),  
 297 the Co *d* states become more symmetric and broaden around the Fermi level, with reduced  
 298 overall spin asymmetry. Additionally, both the O *p* and S *p* states gain intensity within the same



299 energy range. This evolution indicates stronger Co–O and Co–S covalent interactions and  
300 partial delocalization of the Co local moment onto the ligands, which are consistent with the  
301 reduced total magnetic moment of approximately  $1 \mu_B$ . At the atomic level, the local magnetic  
302 moments on the two oxygen atoms are 0.372 and 0.343  $\mu_B$  for O1 and O2, respectively, in the  
303 SP configuration at  $\varepsilon = 4.5\%$ , confirming that both atoms retain significant spin polarization  
304 predominantly in the p orbitals. In the SR configuration at the same strain, these values decrease  
305 to 0.257 and 0.257  $\mu_B$ , consistent with the progressive quenching of the open-shell character  
306 during the SP–SR transition. In other words, the shorter and more covalent Co–O and Co–S  
307 bonds in the SR configuration effectively increase coordination and strengthen the ligand field,  
308 driving a high spin-to-low spin transition at the Co site. Correspondingly, the –pCOHP curves  
309 presented in Figure 3(d) reveal enhanced bonding contributions for Co–O and especially Co–  
310 S bonds, which are accompanied by a modest reduction in the integrated bonding strength of  
311 the O1–O2 bond. These observations agree with the configuration-dependent –ICOHP values  
312 listed in Table 2. Taken together, these results suggest the following causal chain connecting  
313 strain to the regeneration bottleneck. Biaxial tensile strain drives the SP-to-SR structural  
314 transition, in which the subsurface S atom approaches the Co center (Table 1: Co–S decreases  
315 from approximately 3.23 Å to 2.19 Å) and forms a new covalent Co–S bond (Table 2: –ICOHP  
316 increases from 0.097 to 2.038 eV). This increased coordination strengthens the ligand field  
317 around the Co site, as supported by the broadening and increased spin symmetry of the Co *d*  
318 states near  $E_F$ , the enhanced –ICOHP values for the Co–O bonds, and the reduction of the total  
319 magnetic moment from approximately  $3 \mu_B$  to  $1 \mu_B$ , consistent with partial spin-state reduction.  
320 The resulting more covalent and more tightly coordinated Co center simultaneously strengthens  
321 the Co–O interaction and deepens the post-dissociation Co–O–Mo product well. This  
322 strengthened bonding provides an electronic-structure basis for the regeneration penalty



discussed later: the same ligand-field enhancement that promotes  $O_2$  activation also anchors the dissociated oxygen more tightly to the Co center. According to Tables 1, 2 and S1, the observed electronic-structure trends indicate the occurrence of a charge transfer into the antibonding O–O states at the  $Co@V_S$  site and produce a coherent picture of the stronger  $O_2$  activation in the SR configuration as compared with the SP state at  $\varepsilon = 4.5\%$ . These results are consistent with the widely accepted mechanism of  $O_2$  activation via the back-donation into antibonding O–O  $\pi^*$  orbitals. Although our PDOS and COHP analysis results do not explicitly resolve the orbital symmetry, the observed trends strongly support this charge-transfer model.

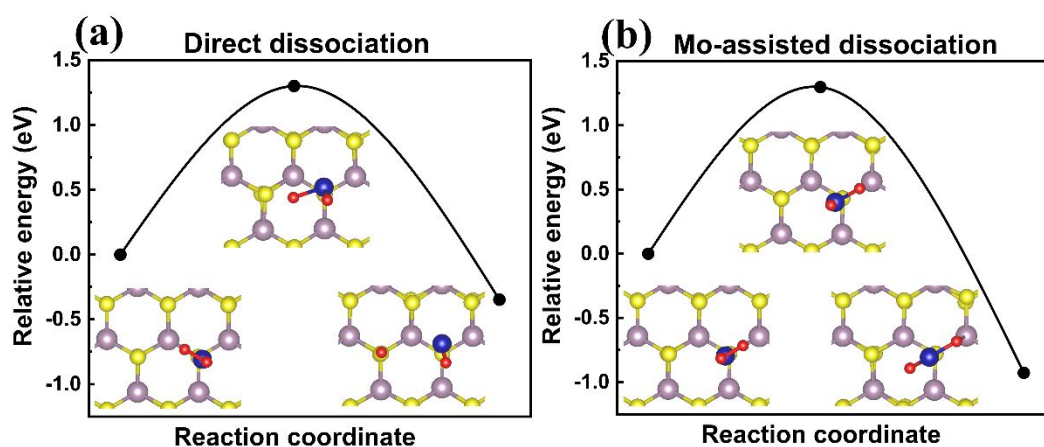


**Figure 4.** Minimum-energy pathways determined for the  $O_2$  dissociation on Co-doped  $MoS_2$  at a zero strain via CI-NEB calculations. (a) “*Direct dissociation*” and (b) “*Mo-assisted dissociation*” pathways.

Before analyzing the strain dependence of O–O dissociation, we first benchmarked our calculations against the reaction pathway previously reported by Zhao et al. for the  $O_2$  molecule adsorbed on a Co-doped  $MoS_2$  monolayer without strain.<sup>15</sup> Along this *direct dissociation*



340 pathway, the O–O bond is cleaved, and the two oxygen atoms ultimately occupy separate  
341 adsorption sites: one atom is bound to the substitutional Co atom, and the other atom is attached  
342 to a neighboring S atom in close agreement with the structural motif proposed by Zhao et al.  
343 As shown in Figure 4(a), our CI–NEB calculation yields an activation barrier of approximately  
344 1.30 eV, which is nearly identical to the literature value of  $\sim 1.33$  eV, confirming that our  
345 computational setup reliably reproduces the established dissociation channel. However, upon  
346 the application of biaxial tensile strain, the minimum-energy path progressively evolves toward  
347 a distinct, *Mo-assisted dissociation* pathway. In this Mo-assisted dissociation pathway, the O–  
348 O bond is cleaved while both oxygen atoms remain coordinated to the Co center; meanwhile,  
349 one oxygen atom forms an additional bridge to the underlying Mo atom, resulting in a  
350 substantially more exothermic Co–O–Mo termination ( $\approx 0.6$  eV more stable than the direct  
351 Co/S termination at  $\varepsilon = 0\%$ ), as illustrated in Figure 4(b). At  $\varepsilon = 0\%$ , the Mo-assisted pathway  
352 exhibits an activation barrier that is essentially identical to that of the direct dissociation  
353 pathway ( $\sim 1.30$  eV for both pathways); however, it leads to a much more exothermic Co–O–  
354 Mo final state ( $\Delta E \approx -0.93$  eV compared with  $-0.35$  eV for the direct pathway; see Figure 4).  
355 Consistently, the total magnetic moment along the Mo-assisted pathway decreases from  $\sim 3 \mu_B$   
356 in the initial superoxo-like state to approximately  $1 \mu_B$  in the Co–O–Mo final state, whereas  
357 the direct pathway retains a larger moment ( $\sim 3 \mu_B$ ) in the Co/S termination, indicating a more  
358 strongly quenched, oxide-like Co–O–Mo configuration in the Mo-assisted case. It is worth  
359 noting that the gas-phase O<sub>2</sub> molecule was computed in its spin-polarized triplet configuration,  
360 consistent with its experimental ground state. The total magnetic moment of approximately  $3$   
361  $\mu_B$  in the initial adsorbed state is consistent with a superoxo-like species retaining substantial  
362 open-shell character and ferromagnetic alignment with the Co center. The progressive  
363 reduction to approximately  $1 \mu_B$  in the Co–O–Mo product state reflects the gradual quenching



364 of this open-shell character as the O–O bond is cleaved, and the oxygen atoms become  
365 incorporated into the lattice. Spin-polarized calculations were employed throughout all NEB  
366 pathways, allowing the magnetic moment to evolve self-consistently along the reaction  
367 coordinate. Because this Mo-assisted final state also becomes the preferred product under the  
368 finite strain and is closely tied to the strain-induced reconstruction of the Co@V<sub>S</sub> site, we focus  
369 on this new pathway in the following analysis of strain-dependent barriers and the electronic  
370 structure. From a catalytic perspective, this alternative Mo-assisted channel is especially  
371 important because it features an activation barrier similar to that of the direct pathway, while  
372 producing a significantly deeper Co–O–Mo product well. This indicates that under the applied  
373 strain, the Mo-assisted pathway becomes the thermodynamically favored channel, effectively  
374 promoting the dissociation process and strongly stabilizing the oxygen species formed on the  
375 catalyst surface.

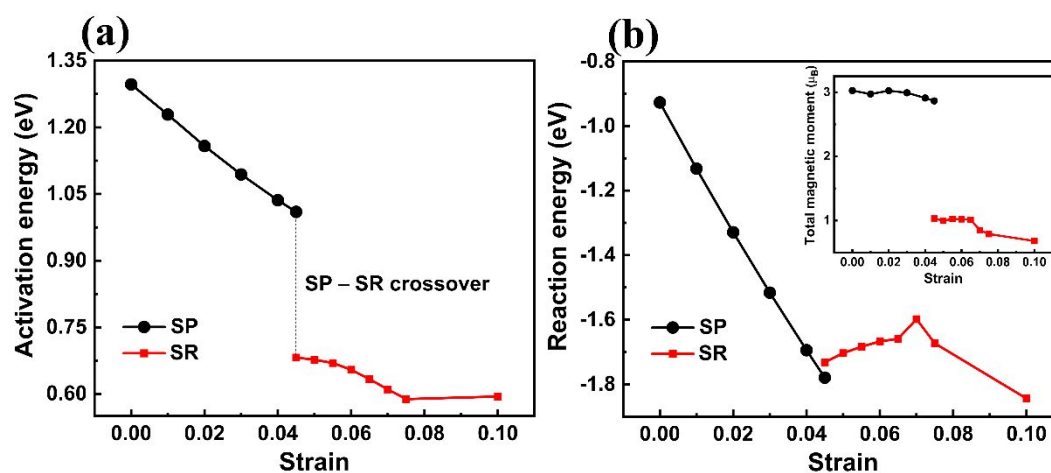
376 The subsequent regeneration analysis focuses on the 4.5–5.5% strain range, as this window  
377 encompasses three qualitatively distinct post-dissociation outcomes observed with increasing  
378 strain: (i) at  $\epsilon \leq 4\%$  (SP branch), O<sub>2</sub> dissociation proceeds along a well-defined pathway with  
379 a progressively decreasing barrier (1.30 to 1.04 eV; Figure 5(a)); (ii) at  $\epsilon = 4.5\text{--}5.0\%$  (SR  
380 branch), the dissociation barrier decreases further to approximately 0.68 eV, but the post-  
381 dissociation oxygen species penetrate subsurface sites, displacing the Co dopant and causing  
382 irreversible structural disruption (Figure S2), with an energetic penalty of approximately +1.15  
383 to +1.23 eV required to escape this penetrated trap (Figure S3); and (iii) at  $\epsilon = 5.5\%$ , a distinct  
384 metastable Co-top O intermediate becomes stable for the first time, enabling the construction  
385 of a well-defined regeneration pathway. This 4.5–5.5% window, therefore, represents the  
386 narrowest range within which the activation–regeneration trade-off transitions from site



387 destruction to a quantifiable kinetic bottleneck, making it the most informative strain window

388 for the subsequent analysis.

389



390

391 **Figure 5.** (a) Activation energy obtained for O<sub>2</sub> dissociation along the Mo-assisted pathway as  
 392 a function of biaxial tensile strain for the SP and SR configurations. The vertical dashed line at  
 393  $\epsilon = 4.5\%$  indicates the SP–SR crossover point. (b) Reaction energy  $\Delta E(\epsilon) = E_{FS}(\epsilon) - E_{IS}(\epsilon)$  per  
 394  $5 \times 3$  MoS<sub>2</sub> supercell, where  $E_{IS}$  and  $E_{FS}$  represent the total energies of the initial adsorbed O<sub>2</sub>  
 395 state and final Co–O–Mo termination at each strain, respectively. The negative values signify  
 396 the exothermic formation of the Co–O–Mo state. In (b), the inset shows the total magnetic  
 397 moment ( $\mu_B$ ) of the initial adsorbed O<sub>2</sub> state as a function of strain; the magnetization decrease  
 398 at the higher strain is consistent with a strain-induced spin reorganization that may contribute  
 399 to the kink in  $\Delta E(\epsilon)$  near  $\epsilon \approx 7\%$ . A more pronounced change in the total magnetic moment is  
 400 also observed for the final Co–O–Mo termination beyond  $\epsilon \approx 7\%$  (not shown here), which is  
 401 consistent with the same kink in  $\Delta E(\epsilon)$ .

402

403 **Table 3.** Strain-dependent Bader charge variations ( $\Delta q$ ) obtained for the substitutional Co  
 404 center and two O atoms in the adsorbed O<sub>2</sub> molecule on Co-doped MoS<sub>2</sub>. Here,  $\Delta q$  is defined  
 405 relative to the neutral atomic valence charges (Co:  $9e$ , O:  $6e$ ) with the positive values indicating



406 electron accumulation and negative values indicating electron depletion. For strains  $\varepsilon \leq 4\%$ ,  
 407 the data correspond to the SP configuration, while for  $\varepsilon \geq 4.5\%$ , they represent the SR  
 408 configuration. At  $\varepsilon = 4.5\%$ , both the metastable SP and thermodynamically favored SR  
 409 structure are included for comparison.

Configuration	Strain	$\Delta q(\text{Co})$	$\Delta q(\text{O1})$	$\Delta q(\text{O2})$
SP	0.000	-0.368	0.331	0.325
	0.020	-0.370	0.324	0.322
	0.040	-0.173	0.295	0.282
	0.045	-0.061	0.294	0.271
SR	0.045	-0.263	0.541	0.180
	0.075	-0.337	0.542	0.043
	0.100	-0.348	0.552	0.068

410  
 411 To quantify how biaxial tensile strain influences the activation of adsorbed  $\text{O}_2$  molecules, we  
 412 calculated minimum-energy paths for O–O dissociation using the climbing-image NEB method.  
 413 Along the SP branch ( $\varepsilon \leq 4\%$ ), the dissociation barrier decreases almost linearly from 1.297 eV  
 414 at  $\varepsilon = 0\%$  to 1.036 eV at  $\varepsilon = 4\%$ , demonstrating that strain facilitates the O–O bond cleavage  
 415 (Figure 5(a)). This reduction coincides with a gradual elongation of the O–O bond from 1.357  
 416 to 1.364 Å and slight shortening of the Co–O distances (Table 1), consistent with the gradual  
 417 weakening and activation of the intramolecular O–O bond under tensile strain, as commonly  
 418 observed for transition metal–dioxygen complexes.<sup>53–55</sup> A qualitatively different regime  
 419 emerges at  $\varepsilon = 4.5\%$ , where the system transitions from the SP to SR configuration. In the SR  
 420 configuration ( $\varepsilon = 4.5\%$ ), the  $\text{O}_2$  dissociation barrier decreases to 0.682 eV and remains at a  
 421 sub-0.7 eV level, reaching  $\sim 0.67$  eV at  $\varepsilon = 5.5\%$  (Figure 5(a)). This reduction is associated with  
 422 the (i) formation of shorter Co–O bonds with lengths of approximately 1.83 Å and (ii) further



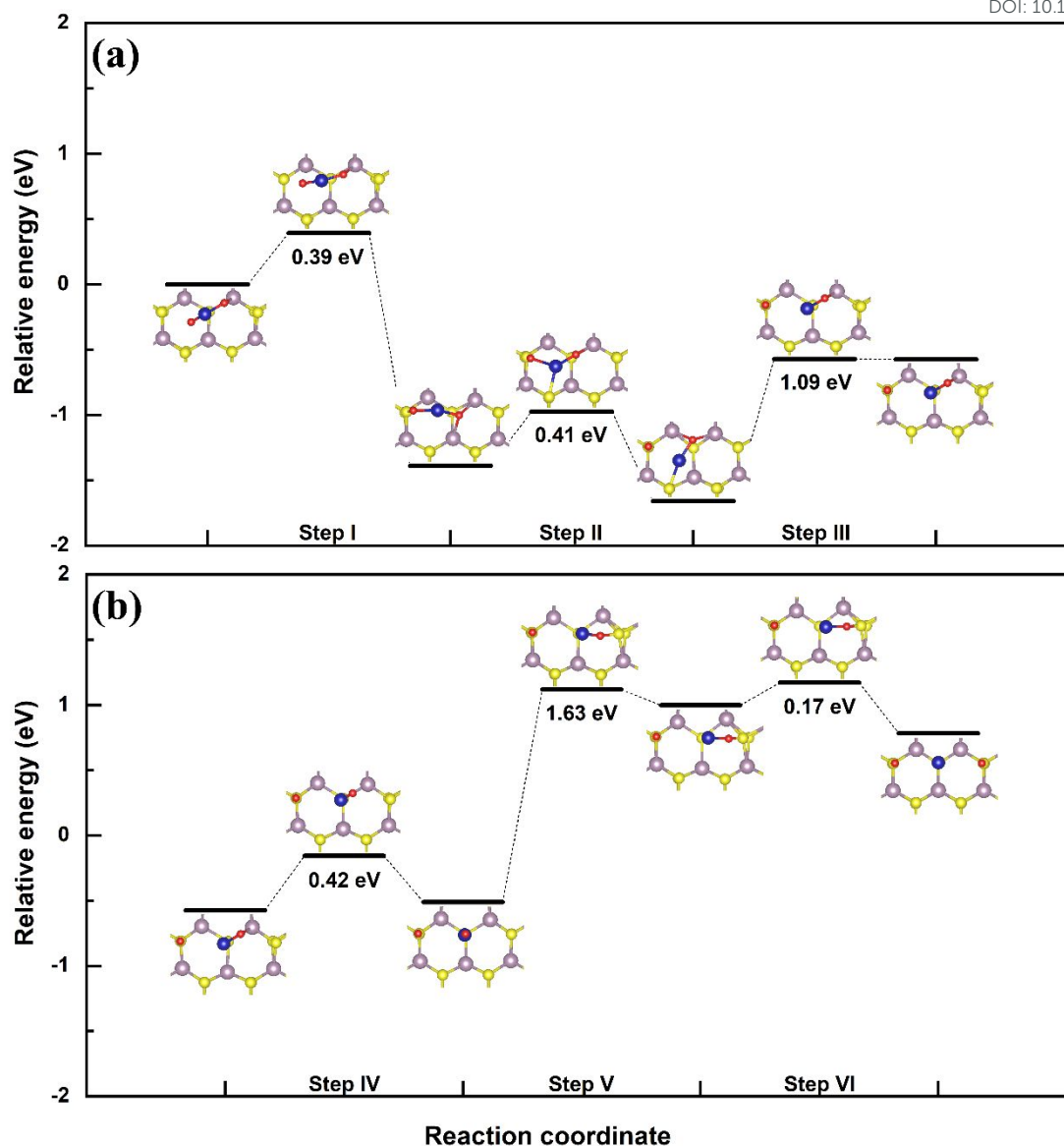
423 elongation of the O–O bond to 1.380 Å as compared with that in the SP configuration. Bader  
424 charge analysis (Table 3) shows that the net charge on the O<sub>2</sub> moiety remains around ~0.6–0.7  
425 *e* across the studied strain range. However, the SR configuration at  $\epsilon = 4.5\%$  exhibits  
426 pronounced intramolecular charge asymmetry ( $\Delta q(\text{O1}) \approx 0.54 e$  and  $\Delta q(\text{O2}) \approx 0.18 e$ ),  
427 indicating an electronically asymmetric superoxo-like O<sub>2</sub> species with the charge preferentially  
428 localized on one oxygen atom. Along the SP branch ( $\epsilon \leq 4\%$ ), the Co center is gradually  
429 reduced as  $\Delta q(\text{Co})$  increases from  $-0.37 e$  to  $-0.17 e$ . Upon transitioning to the SR state at  $\epsilon =$   
430  $4.5\%$ ,  $\Delta q(\text{Co})$  becomes more negative again ( $\approx -0.26 e$ ), indicating a partial reoxidation of Co  
431 accompanied by the pronounced intramolecular charge asymmetry within O<sub>2</sub>. Although the  
432 total Bader charge on O<sub>2</sub> increases moderately from approximately 0.58 *e* at  $\epsilon = 4\%$  (SP) to  
433 0.72 *e* at  $\epsilon = 4.5\%$  (SR), this change is small compared with the large charge imbalance between  
434 O1 and O2. This suggests that the SP–SR transition primarily redistributes charges between Co  
435 and the two O atoms rather than significantly altering the overall reduction level of O<sub>2</sub>. These  
436 findings reveal two distinct activation regimes: at  $\epsilon \leq 4\%$ , biaxial tension induces continuous  
437 mechanochemical activation within the SP configuration, whereas at  $\epsilon = 4.5\%$ , a substrate-  
438 mediated reconstruction to the SR configuration creates a new initial state, in which  
439 cooperative structural and electronic rearrangements synergistically lower the O<sub>2</sub> dissociation  
440 barrier. In addition to the barrier heights, we examined the strain dependence of the reaction  
441 energy,  $\Delta E(\epsilon) = E_{\text{FS}}(\epsilon) - E_{\text{IS}}(\epsilon)$ , per 5×3 supercell (Figure 5(b)), where  $E_{\text{IS}}$  and  $E_{\text{FS}}$  denote the  
442 total energies of the initial adsorbed O<sub>2</sub> state and final Co–O–Mo termination along the same  
443 Mo-assisted pathway at each strain, respectively. Along the SR branch, the reaction energy  
444 first gradually increases (becomes less exothermic) between  $\epsilon = 4.5\%$  and 6.5% and then  
445 exhibits a small kink around  $\epsilon \approx 7\%$ , (Figure 5(b)), after which it decreases again toward more  
446 exothermic values at higher strains. At this point, the total magnetic moment of the final Co–



447 O–Mo state changes from approximately  $1 \mu_B$  at lower strains to approximately  $0.4 \mu_B$  at  $\epsilon \approx$   
448 7%. This spin-state rearrangement slightly modifies the total energy of the product state,  
449 producing the kink depicted in Figure 5(b). Nevertheless,  $O_2$  dissociation remains strongly  
450 exothermic ( $\Delta E \approx -1.6$  to  $-1.8$  eV) along the entire SR branch, reinforcing the conclusion that  
451 the Mo-assisted pathway leads to a deeply stabilized Co–O–Mo termination under strain. From  
452 a catalytic perspective, such a deep and strongly exothermic Co–O–Mo termination suggests  
453 that the Co@V<sub>S</sub> site is likely thermodynamically trapped in this O-rich state under strain. An  
454 analysis of the regeneration pathway (see below) shows that this excessive stabilization  
455 imposes a significant energy penalty for removing the oxygen species, thereby hindering the  
456 reactivation process. Overall, these findings reveal two distinct regimes of  $O_2$  activation at  
457 Co@V<sub>S</sub>: a strain-driven mechanochemical activation along the SP branch ( $\epsilon \leq 4\%$ ), and a  
458 reconstruction-driven regime for  $\epsilon \geq 4.5\%$ , in which the SR configuration and resulting Co–O–  
459 Mo termination work synergistically to lower the dissociation barrier while strongly stabilizing  
460 the dissociated oxygen species through the formation of robust Co–O and Mo–O bonds.

461





462  
 463 **Figure 6.** Minimum-energy pathway obtained for regenerating the clean Co@V<sub>S</sub> site from the  
 464 Co–O–Mo-terminated intermediate under a biaxial tensile strain of  $\varepsilon = 5.5\%$  (SR) by  
 465 performing CI-NEB calculations. (a) Co-site rearrangement following O<sub>2</sub> dissociation (Steps  
 466 I–III). (b) Oxygen hopping from the Co site to a neighboring S site (Steps IV–VI). Energies  
 467 are referenced to the initial state of Step I ( $E = 0$ ) with the final state of each step serving as the  
 468 initial state for the subsequent step. The activation barriers determined for Steps I–VI via the  
 469 formula  $E_a = E_{TS} - E_{IS}$  are 0.39, 0.41, 1.09, 0.42, 1.63, and 0.17 eV, respectively. Representative  
 470 initial, transition, and final structures are shown for each step.

471



472 It was found that the Mo-assisted dissociation pathway led to a highly stabilized Co–O–Mo  
473 termination. Notably, additional structural optimizations conducted at lower strains ( $\epsilon = 4.5$ –  
474  $5.0\%$ ) demonstrated that the remaining oxygen atom tended to diffuse into the MoS<sub>2</sub> lattice,  
475 displacing the Co dopant and resulting in the formation of a disordered oxide-like structure  
476 (Figure S2). Furthermore, escaping from this penetrated Co–O–Mo trap to representative  
477 “recovery” endpoints is a strongly endothermic process ( $\Delta E \approx +1.15$  eV for Co-top; see Figure  
478 S3), indicating a deep thermodynamic trap and the existence of substantial kinetic barriers.  
479 Because such structural disruption complicates the recovery of the original single-atom site,  
480 we focused our regeneration analysis on the higher-strain regime, in which the active site  
481 remained intact. Experimentally, biaxial tensile strains up to approximately  $5.6\%$  have been  
482 achieved in suspended monolayer MoS<sub>2</sub> membranes through pressure-induced bulging,  
483 establishing a practical feasibility limit for strain engineering in free-standing geometries.<sup>29</sup>  
484 Consequently, we concentrated on regeneration kinetics and energetics within this feasible  
485 range ( $\epsilon \approx 5$ – $6\%$ ). Here, we defined active-site regeneration as the removal or relocation of  
486 dissociation-derived O species from the Co center via lateral lattice-oxygen migration, which  
487 serves as a proxy for the intrinsic difficulty of recovering the Co coordination environment.  
488 Although this proxy does not explicitly account for the electrode potential, solvent effects, or  
489 proton–electron transfer, it provides a consistent measure of the intrinsic kinetic barrier to  
490 reopening the Co coordination environment after O<sub>2</sub> dissociation—an essential prerequisite for  
491 the sustained catalytic turnover. To evaluate this proxy, we constructed a well-defined  
492 minimum-energy pathway from the results of CI–NEB calculations, consisting of Steps I–III  
493 (Figure 6(a)) and Steps IV–VI (Figure 6(b)). We selected  $\epsilon = 5.5\%$  (SR) as a representative  
494 condition, where the active site remains intact and O<sub>2</sub> dissociation is strongly facilitated ( $E_a$  for  
495 O<sub>2</sub> dissociation  $\approx 0.67$  eV). At lower strains ( $\epsilon = 4.5$ – $5.0\%$ ), the Step III endpoint (Co-top O



intermediate) cannot be stabilized, preventing the formation of a well-defined intermediate that bridges the subsequent lateral-migration steps. Therefore, we focus on  $\varepsilon = 5.5\%$ , at which the Step III intermediate becomes a distinct metastable minimum, allowing the regeneration pathway to be consistently defined. Accordingly, we constructed the regeneration pathway starting from the fully dissociated Co–O–Mo product state at  $\varepsilon = 5.5\%$  in the SR configuration (Figure 6). Initially, the two oxygen atoms form an O–Co–O–Mo configuration: one O atom bridges Co and a neighboring S atom, while the other O atom binds to both Co and an underlying Mo atom. This minimum-energy path involves six elementary oxygen-migration steps (Steps I–VI). The final state of each step is used as the initial state of the subsequent step. In the first step, the outer O atom breaks its Co–O bond and migrates to a nearby S adsorption site, creating a terminal O atom bound to a surface S site and leaving a single Co–O–Mo linkage. In the second step, the remaining O atom detaches from the Mo site and moves upward toward the Co center, forming a Co–O species oriented closer to the surface normal at the Co-top site. In the third step, the Co-bound oxygen undergoes further rearrangement along the minimum-energy path, maintaining the Co-top O motif before the lateral diffusion. This Step III intermediate represents a distinct strain-dependent metastable minimum that becomes stable only at  $\varepsilon \geq 5.5\%$ . At lower strains ( $\varepsilon = 4.5\text{--}5.0\%$ ), it relaxes into a different oxide-like configuration, consistent with the active-site disruption behavior discussed above. Therefore, Step III acts as a preparatory rearrangement that preserves the Co-top O motif and establishes a local geometry for the subsequent lateral migration steps (Steps IV–VI). In the fourth step, the Co-bound oxygen moves (hops) from the Co-top position toward a neighboring S site, forming an intermediate configuration in which the O atom is laterally displaced away from the Co center but continues to interact with it. During the fifth step, the Co-bound oxygen undergoes the rate-limiting lateral migration away from the Co center toward the neighboring



520 S site, substantially weakening—but not completely eliminating—the residual Co–O  
521 interaction. Finally, in the sixth step, this remaining weak Co–O interaction is fully released,  
522 resulting in a clean Co@VS site coordinated solely by the MoS<sub>2</sub> lattice, with two terminal O-  
523 on-S species nearby. The energy profile presented in Figure 6 indicates that the initial migration  
524 steps (Steps I–III) have moderate activation barriers of 0.39, 0.41, and 1.09 eV, respectively.  
525 The subsequent oxygen-removal stage (Steps IV–VI) features a moderate barrier in Step IV  
526 (0.42 eV), high barrier in Step V (1.63 eV), and small final barrier in Step VI (0.17 eV).  
527 Importantly, in Step II, the transition and final states are nearly isoenergetic, resulting in a small  
528 reverse barrier ( $E_{TS} - E_{FS}$ ) and thus a non-negligible probability of back-migration under  
529 thermal fluctuations. Additionally, the rate-determining barrier in Step V (1.63 eV) is more  
530 than two times greater than that of the unstrained system (~0.77 eV; Figure S4), indicating that  
531 the strain-induced stabilization of the Co–O bond substantially hinders oxygen diffusion. This  
532 finding is in good agreement with the larger (more bonding) –ICOHP values for the Co–O  
533 bond listed in Table S2. Furthermore, the overall regeneration process is strongly endothermic,  
534 with the final state ~2.20 eV higher than the initial Co–O–Mo state, reinforcing the  
535 thermodynamic penalty that deepens the kinetic bottleneck in Step V. Hence, in the lattice-  
536 oxygen migration proxy pathway considered herein, tensile strain strengthens the Co–O  
537 interaction and elevates the barrier for the lateral oxygen diffusion, thereby hindering the  
538 regeneration of the clean Co@V<sub>S</sub> site even after the strain-enhanced O<sub>2</sub> activation. Consistent  
539 with the deep thermodynamic trapping illustrated in Figure 5, this phenomenon may imply  
540 persistent oxygen coverage and highlights a critical trade-off between facile O<sub>2</sub> dissociation  
541 and challenging site reactivation in strain-engineered single-atom catalysts.

542



543 **4. Conclusions**

544 In this study, we performed spin-polarized DFT calculations to explore how strain affected the  
545 O<sub>2</sub> activation and regeneration mechanisms in Co-doped MoS<sub>2</sub> (Co@V<sub>S</sub>). The obtained results  
546 revealed that applying biaxial tensile strain triggered a structural transition from the SP to an  
547 SR configuration at a strain of approximately 4.5%, serving as a critical switch that enhanced  
548 O<sub>2</sub> activation. Although the strain-induced SR configuration significantly lowered the  
549 dissociation barrier via a Mo-assisted pathway, catalyst regeneration remains a significant  
550 challenge owing to the concurrent strengthening of the Co–O interaction under the applied  
551 strain. Specifically, we identified two strain-dependent regeneration failure modes: at  $\epsilon = 4.5\text{--}$   
552  $5.0\%$ , the dissociation-derived oxygen species penetrate subsurface sites, displacing Co atoms  
553 and hindering the site recovery; at  $\epsilon = 5.5\%$ , the Co@V<sub>S</sub> structure remains intact, but the  
554 oxygen removal process is limited by the lateral diffusion barrier of 1.63 eV (Step V), which  
555 is more than twice as high as the barrier in the unstrained case ( $\sim 0.77$  eV; Figure S4). This  
556 diffusion bottleneck is followed by the small final barrier of 0.17 eV (Step VI). These findings  
557 highlight a notable trade-off: while tensile strain effectively promotes O<sub>2</sub> dissociation, it also  
558 stabilizes the oxide-like product states and increases the kinetic difficulty of the oxygen  
559 removal process, making active-site regeneration a likely bottleneck within the regeneration  
560 (lattice-oxygen migration) pathway studied in this work. More broadly, this activation–  
561 regeneration trade-off may apply to other strain-engineered single-atom catalysts, for which O<sub>2</sub>  
562 activation correlates with stronger metal–oxygen bonding. Accordingly, our study suggests that  
563 future catalyst designs should carefully balance activation kinetics with the kinetic feasibility  
564 of regeneration to overcome this intrinsic limitation. It should be noted that the lattice-oxygen  
565 migration proxy adopted herein does not incorporate electrode potential, solvation, or proton–



566 electron transfer steps; therefore, the absolute regeneration barriers may shift under realistic  
567 electrochemical conditions. PBE+U sensitivity tests ( $U_{\text{eff}} = 3.3$  eV; Table S3) indicate that the  
568 SP–SR crossover strain shifts to higher values with the Hubbard correction, while the SR  
569 metastable minimum and the monotonic strain-dependent trend are preserved, supporting the  
570 qualitative robustness of the conclusions. Nevertheless, the qualitative activation–regeneration  
571 trade-off identified in this work may persist, as it originates from the fundamental strain-  
572 induced strengthening of Co–O and Mo–O bonds. Under applied electrochemical potential, the  
573 absolute regeneration barriers may shift in either direction depending on the specific potential,  
574 solvation environment, and proton-coupled reaction steps; thus, the barrier values reported here  
575 should be interpreted as baseline structural references rather than operando predictions.  
576 Coupling the present structural framework with explicit electrochemical models, such as the  
577 computational hydrogen electrode or implicit solvation approaches, represents an important  
578 direction for future work.

579 Finally, achieving uniform biaxial tensile strain under catalytic operating conditions remains  
580 experimentally challenging, although strains of approximately 5.6% have been demonstrated  
581 in suspended monolayer MoS<sub>2</sub> membranes<sup>29</sup> and breaking strains of 6–11% have been reported  
582 during nanoindentation.<sup>52</sup> The present study, therefore, serves as a computational reference  
583 framework that identifies the mechanistic transitions governing the activation–regeneration  
584 balance; the insights may remain qualitatively relevant for any strain modality that produces  
585 comparable lattice expansion near the active site. The electronic-structure analysis relied on  
586 PDOS, COHP, and Bader charge methods, which provide atom- and bond-resolved insight into  
587 localized defect states; complementary band structure calculations could further clarify the  
588 dispersion of these states and represent a valuable direction for future investigation.



589

590 **Author contributions**

591 **Soon-Dong Park:** Conceptualization, Methodology, Software, Investigation, Visualization,  
592 Writing – Original Draft

593 **Sung Youb Kim:** Writing - Review & Editing, Supervision, Project administration, Funding  
594 acquisition

595

596 **Conflicts of interest**

597 There are no conflicts to declare.

598

599 **Data availability**

600 The data supporting this study—including NEB pathways, energies, and numerical data for  
601 plots—are provided in the Electronic Supplementary Information (ESI). Atomic structure files,  
602 additional input files, and analysis scripts can be obtained from the corresponding author upon  
603 reasonable request. References cited in the ESI are included in the article's reference list.

604

605 **Acknowledgements**

606 We gratefully acknowledge support from the Basic Research Laboratory program of the  
607 National Research Foundation of Korea (Grant No. 2021RA4A1033224) and the UNIST  
608 Supercomputing Center for providing access to supercomputing resources. This work was also  
609 supported by the InnoCORE program of the Ministry of Science and ICT (N10250154). The



610 authors reviewed and edited the content thoroughly and took full responsibility for the final  
611 manuscript.

612

### 613 **Supplementary data**

614 Electronic supplementary information (ESI) available: Figure S1–S4, Tables S1–S3.

615

### 616 **References**

- 617 1 X. Chia, A. Y. S. Eng, A. Ambrosi, S. M. Tan and M. Pumera, *Chem. Rev.*, 2015, **115**,  
618 11941–11966.
- 619 2 S. Zhao, K. Wang, X. Zou, L. Gan, H. Du, C. Xu, F. Kang, W. Duan and J. Li, *Nano*  
620 *Res.*, 2019, **12**, 925–930.
- 621 3 N. Karmodak, L. Bursi and O. Andreussi, *J. Phys. Chem. Lett.*, 2022, **13**, 58–65.
- 622 4 Y. Yan, S. Liang, X. Wang, M. Zhang, S. M. Hao, X. Cui, Z. Li and Z. Lin, *Proc. Natl.*  
623 *Acad. Sci. U. S. A.*, 2021, **118**, e21110036118.
- 624 5 M. Wang, X. Huang, Z. Yu, P. Zhang, C. Zhai, H. Song, J. Xu and K. Chen,  
625 *Nanomaterials*, 2022, **12**, 4069.
- 626 6 S. Xin, Z. Liu, L. Ma, Y. Sun, C. Xiao, F. Li and Y. Du, *Nano Res.*, 2016, **9**, 3795–3811.
- 627 7 S. Pan, Z. Cai, Y. Duan, L. Yang, B. Tang, B. Jing, Y. Dai, X. Xu and J. Zou, *Appl.*  
628 *Catal. B Environ.*, 2017, **219**, 18–29.
- 629 8 J. Tang, C. Wang, H. Zhang and J. Guo, *J. Alloys Compd.*, 2022, **911**, 164991.
- 630 9 J. H. Kim, J. G. Lee and M. J. Choi, *Materials (Basel)*, 2024, **17**, 4277.
- 631 10 L. Fan, X. Dai, F. Li, X. Li, Z. Liu, Q. Guo, C. Zhang, Z. Kang and D. Sun, *J. Mater.*  
632 *Sci. Technol.*, 2025, **226**, 1–11.



- 633 11 L. Zhang, Y. Dong, L. Li, Y. Shi, Y. Zhang, L. Wei, C. L. Dong, Z. Lin and J. Su, *Nano-*  
634 *Micro Lett.*, 2025, **17**, 88.
- 635 12 D. Xu, J. Jiang, D. Liu, X. Wei, J. Yang, Z. Zhuang, Y. Dou, X. Liu, J. Duan and D.  
636 Wang, *Microstructures*, 2026, **6**, 2026020.
- 637 13 C. Ataca and S. Ciraci, *J. Phys. Chem. C*, 2011, **115**, 13303–13311.
- 638 14 D. Ma, W. Ju, T. Li, X. Zhang, C. He, B. Ma, Y. Tang, Z. Lu and Z. Yang, *Appl. Surf.*  
639 *Sci.*, 2016, **364**, 181–189.
- 640 15 B. Zhao, L. L. Liu, G. D. Cheng, T. Li, N. Qi, Z. Q. Chen and Z. Tang, *Mater. Des.*,  
641 2017, **113**, 1–8.
- 642 16 W. Zhou, X. Zou, S. Najmaei, Z. Liu, Y. Shi, J. Kong, J. Lou, P. M. Ajayan, B. I.  
643 Yakobson and J. C. Idrobo, *Nano Lett.*, 2013, **13**, 2615–2622.
- 644 17 S. Najmaei, Z. Liu, W. Zhou, X. Zou, G. Shi, S. Lei, B. I. Yakobson, J. C. Idrobo, P. M.  
645 Ajayan and J. Lou, *Nat. Mater.*, 2013, **12**, 754–759.
- 646 18 S. Kc, R. C. Longo, R. M. Wallace and K. Cho, *J. Appl. Phys.*, 2015, **117**, 135301.
- 647 19 A. Wu, Q. Song and H. Liu, *Comput. Theor. Chem.*, 2020, **1187**, 112906.
- 648 20 H. Lu, A. Kummel and J. Robertson, *APL Mater.*, 2018, **6**, 066104.
- 649 21 X. Zhang, J. Xu, A. Zhi, J. Wang, Y. Wang, W. Zhu, X. Han and K. Wang, *Adv. Sci.*,  
650 2024, **11**, 2408640.
- 651 22 K. Dolui, I. Rungger, C. Das Pemmaraju and S. Sanvito, *Phys. Rev. B*, 2013, **88**, 075420.
- 652 23 H. P. Komsa and A. V. Krasheninnikov, *Phys. Rev. B*, 2015, **91**, 125304.
- 653 24 M. Li, T. Li and Y. Jing, *RSC Adv.*, 2022, **12**, 31525–31534.
- 654 25 G. Liu, A. W. Robertson, M. M. Li, W. C. H. Kuo, M. T. Darby, M. H. Muhieddine, Y.  
655 Lin, K. Suenaga, M. Stamatakis and J. H. Warner, *Nat. Chem.*, 2017, **9**, 810–816.
- 656 26 W. T. Yein, D. Kim and Q. Wang, *Chem. Proc.*, 2024, **15**, 3.
- 657 27 T. Li, *Phys. Rev. B*, 2012, **85**, 235407.
- 658 28 H. J. Conley, B. Wang, J. I. Ziegler, R. F. Haglund, S. T. Pantelides and K. I. Bolotin,  
659 *Nano Lett.*, 2013, **13**, 3626–3630.



- 660 29 D. Lloyd, X. Liu, J. W. Christopher, L. Cantley, A. Wadehra, B. L. Kim, B. B. Goldberg,  
661 A. K. Swan and J. S. Bunch, *Nano Lett.*, 2016, **16**, 5836–5841.
- 662 30 R. Frisenda, M. Drüppel, R. Schmidt, S. Michaelis de Vasconcellos, D. Perez de Lara,  
663 R. Bratschitsch, M. Rohlfing and A. Castellanos-Gomez, *npj 2D Mater. Appl.*, 2017, **1**,  
664 10.
- 665 31 W. S. Yun, S. W. Han, S. C. Hong, I. G. Kim and J. D. Lee, *Phys. Rev. B*, 2012, **85**,  
666 033305.
- 667 32 S.-D. Park and S. Y. Kim, *Coupled Syst. Mech.*, 2016, **5**, 305–314.
- 668 33 P. E. Blöchl, *Phys. Rev. B*, 1994, **50**, 17953–17979.
- 669 34 G. Kresse and D. Joubert, *Phys. Rev. B*, 1999, **59**, 1758.
- 670 35 G. Kresse and J. Furthmüller, *Phys. Rev. B*, 1996, **54**, 11169–11186.
- 671 36 G. Kresse and J. Furthmüller, *Comput. Mater. Sci.*, 1996, **6**, 15–50.
- 672 37 J. P. Perdew, K. Burke and M. Ernzerhof, *Phys. Rev. Lett.*, 1996, **77**, 3865.
- 673 38 H. J. Monkhorst and J. D. Pack, *Phys. Rev. B*, 1976, **13**, 5188.
- 674 39 R. Dronskowski and P. E. Bloechl, *J. Phys. Chem.*, 1993, **97**, 8617–8624.
- 675 40 A. Togo and I. Tanaka, *Scr. Mater.*, 2015, **108**, 1–5.
- 676 41 A. Togo, L. Chaput, T. Tadano and I. Tanaka, *J. Phys. Condens. Matter*, 2023, **35**,  
677 353001.
- 678 42 G. Henkelman, A. Arnaldsson and H. Jónsson, *Comput. Mater. Sci.*, 2006, **36**, 354–360.
- 679 43 E. Sanville, S. D. Kenny, R. Smith and G. Henkelman, *J. Comput. Chem.*, 2007, **28**,  
680 899–908.
- 681 44 W. Tang, E. Sanville and G. Henkelman, *J. Phys. Condens. Matter*, 2009, **21**, 084204.
- 682 45 S. Maintz, V. L. Deringer, A. L. Tchougréeff and R. Dronskowski, *J. Comput. Chem.*,  
683 2016, **37**, 1030–1035.
- 684 46 H. Jónsson, G. Mills and K. W. Jacobsen, in *Classical and Quantum Dynamics in*  
685 *Condensed Phase Simulations*, World Scientific, 1998, pp. 385–404.
- 686 47 G. Henkelman and H. Jónsson, *J. Chem. Phys.*, 2000, **113**, 9978–9985.



View Article Online  
DOI: 10.1039/D6TA01659F

- 687 48 G. Henkelman, B. P. Uberuaga and H. Jónsson, *J. Chem. Phys.*, 2000, **113**, 9901–9904.
- 688 49 N. K. Oh, J. Seo, S. Lee, H. J. Kim, U. Kim, J. Lee, Y. K. Han and H. Park, *Nat.*  
689 *Commun.*, 2021, **12**, 4606.
- 690 50 A. Grimaud, O. Diaz-Morales, B. Han, W. T. Hong, Y. L. Lee, L. Giordano, K. A.  
691 Stoerzinger, M. T. M. Koper and Y. Shao-Horn, *Nat. Chem.*, 2017, **9**, 457–465.
- 692 51 R. C. Cooper, J. W. Kysar and C. A. Marianetti, *Phys. Rev. B*, 2014, **90**, 167401.
- 693 52 S. Bertolazzi, J. Brivio and A. Kis, *ACS Nano*, 2011, **5**, 9703–9709.
- 694 53 P. H. Krupenie, *J. Phys. Chem. Ref. Data*, 1972, **1**, 423–534.
- 695 54 C. J. Cramer, W. B. Tolman, K. H. Theopold and A. L. Rheingold, *Proc. Natl. Acad.*  
696 *Sci. U. S. A.*, 2003, **100**, 3635–3640.
- 697 55 M. M. Montemore, M. A. Van Spronsen, R. J. Madix and C. M. Friend, *Chem. Rev.*,  
698 2018, **118**, 2816–2862.
- 699



The data supporting this study—including NEB pathways, energies, and numerical data for plots—are provided in the Electronic Supplementary Information (ESI). Atomic structure files, additional input files, and analysis scripts can be obtained from the corresponding author upon reasonable request.

References cited in the ESI are included in the article's reference list.

